Section 4

Parameterization of important atmospheric and surface processes, effects of different parameterizations

Modeling Interannual Variability of $\delta^{18}O$ of Atmospheric CO_2 and its Dependence on Humidity and Isotope Hydrology

Nikolaus Buenning[1], David Noone[1], William Riley[2], Christopher Still[3], James Randerson[4], Lisa Welp[5], James White[6], Bruce Vaughn[6], John Miller[1], Pieter Tans[1]

1 Cooperative Institute of Research in Environmental Sciences, University of Colorado, Boulder, CO, USA
2Earth Sciences Division Lawrence, Berkeley National Laboratory, Berkeley, CA, USA
3Geography Department, University of California, Santa Barbara, CA, USA
4Department of Earth System Science, University of California, Irvine, CA, USA
5. Yale School of Forestry and Environmental Science
6. Institute of Arctic and Alpine Research, University of Colorado, Boulder
(Email: buenning@colorado.edu)

Measurements of the abundance of $CO^{18}O$ in the atmosphere (denoted hereafter as $\delta^{18}O=(R/R_{Standard}-1) \times 1000$, where R is the mole ratio of heavy to light isotopes) at the NOAA/ESRL baseline observatories have shown a gradual downward trend during a period from the early 1990s until the late 1990s. This downward trend is then followed by a recovery period, and then another decline up to present day (solid line in Figure 1). It is believed that fluxes from the terrestrial biosphere largely influence changes in $\delta^{18}O$-CO_2, with photosynthetic fluxes enriching the atmosphere in $CO^{18}O$ and respiratory fluxes depleting it. However the interannual changes could also be a consequence of changes in the isotopic composition of the fluxes. The fluxes from the leaves and the soils take on the isotopic composition of the terrestrial water pools with which CO_2 interacts. There are a number of factors that affect the isotopic composition of both soil and leaf water, including the isotope input from precipitation and water vapor. A steady state model based on the Craig-Gordon (1986) method would suggest that the water pools are largely influenced by relative humidity. While an increase in humidity would increase stomatal conductance and in turn increase biospheric productivity, it also will cause leaves to take in more of the isotopically light water vapor, causing the leaf water to become less enriched with the heavy ^{18}O isotope. Thus, isotope modeling provides a critical test of the humidity estimate in the reanalysis datasets and in climate models.

To model the interannual variability of $\delta^{18}O$-CO_2, we use an isotopic version of the NCAR Land Surface Model (ISOLSM, Bonan, 1996; Riley et al., 2002) to simulate the isotopic composition of the water pools as well as the terrestrial CO_2 fluxes. ISOLSM is forced with meteorological data produced by Dai (2006) for the years 1979-2004, and the $\delta^{18}O$ values of precipitation and water vapor are prescribed from the MU-GCM monthly climatology (Noone and Simmonds, 2002). Fluxes from the oceans, biomass burning, and fossil fuel burning are taken from various datasets, with no interannual variability. All of these fluxes are then put into the NCAR Community Atmosphere Model (CAM) to model $\delta^{18}O$-CO_2 and its interannual variability. In additional to an unperturbed control simulation, two perturbations are conducted. To examine the affects of humidity changes, the model is forced with artificially imposed relative humidity variations in the form of sine wave with an anomaly of ±5% about the long term mean. Another simulation is conducted with artificially imposed variations in the $\delta^{18}O$ value of precipitation of water vapor; again in the form of a sine wave and with a ±1‰ amplitude.

Figure 1 shows these results for the gridcell close to Mauna Loa, along with the observed annual means. Results from the control simulation show very small changes relative to the observations, and the overall shape of interannual variations do not match up with the Mauna Loa observations. These results could suggest that there are very small, and unrealistic, interannual humidity variations in the reanalysis dataset that is used to force ISOLSM. However, the simulations with artificially imposed anomalies in humidity and isotope hydrology, show large interannual variations. In fact, the imposed variations were more than enough to explain the changes seen in the observations. Results from the control simulation would indicate that there is not enough year-to-year change in relative humidity to cause large $\delta^{18}O$-CO_2 variations. However, humidity records at several stations in Southeast Asia show an upward trend during the 1990s, which is consistent with the observed trend in the $\delta^{18}O$ value of atmospheric CO_2. These station observations suggest that the reanalysis does not capture the true humidity variations that were observed during this period. Similarly, interannual changes in $\delta^{18}O$ of precipitation at Bangkok and Darwin also match up well with $\delta^{18}O$-CO_2 observations. So since $\delta^{18}O$-CO_2 is sensitive to even relatively modest variations in humidity, these results show that the reanalysis data has unrealistically low variability in near-surface relative humidity.

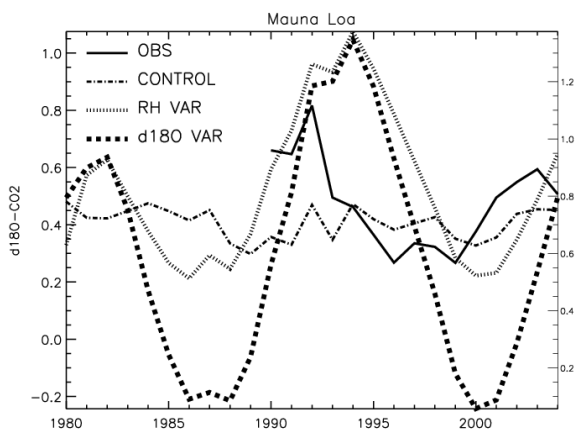

Figure 1. Annual mean of $\delta^{18}O$-CO_2 observed at Mauna Loa (solid line), and for the control simulation (dash-dot), humidity anomaly simulation (hashed line), and isotope hydrology anomaly run (dashed)

Bonan, G., 1996: A land surface model (LSM version 1.0) for ecological, hydrological, and atmospheric studies: Technical description and user's guide, TN-417+STR, Natl. Cent. For Atmos. Res., Boulder, CO.

Craig, H., and Gordon A., 1965. Deterium and Oxygen-18 variations in the ocean and the marine atmosphere. In: *Stable isotopes in oceanic studies and paleotemperatures* (ed. Laboratory of Geology and Nuclear Sciences), Pisa, Italy.

Dai, A., 2006: Recent climatology, variability and trends in global surface humidity. *J. Climate*, 19, 3589–3606.

Noone, D., and Simmonds, I., 2002: Associations between • 18O of water and climate parameters in a simulation of atmospheric circulation for 1979-1995. *J. Climate* **15(22)**, 3140-3169.

Riley, W. J., Still, C. J., Torn, M., and Berry, J. A., 2002: A mechanistic model of $H_2{}^{18}O$ and $C^{18}OO$ fluxes between ecosystems and atmosphere: model description a sensitivity analyses. *Global Biogeochem. Cycles* **16**, 1095-1108.

THE METHOD OF THE CLOUD – RADIATION INTERACTION DESCRIPTION FOR THE ATMOSPHERIC HYDRODYNAMICAL MODEL

Dmitrieva – Arrago L.R., Shatunova M.V.

Hydrometeorological Research Center of Russia, Russia

dmitrieva@mecom.ru

The delta – Eddington approximation to the radiation transfer equation solution is used for the solar radiation fluxes calculations. The developed algorithm is presented in (*Dmitirieva-Arrago, Shatunova, 2001*). The main problem of the radiation fluxes calculation is the influence of the cloudiness, its spreading and microphysical properties. Microphysical properties define the cloud optical characteristics – the albedo and transmission and the fluxes at the surface. To receive the microphysical characteristics the humidity transformation model that include the cloud water content transfer equation is used (*Dmitrieva-Arrago, 2004 a,b*). As a result of model integration space distribution of cloud water content and mean cloud particle radius are obtained. The clouds optical properties are defined by the value of the cloud absorption (σ_{abs}) and extinction (σ_{ext}) coefficients.

Mentioned coefficients are calculated by the following formulas (*van de Hulst, 1957*):

$$\sigma_{ext} = \pi \int_0^\infty r^2 Q_{ext} n(r) dr, \tag{1}$$

$$\sigma_{abs} = \pi \int_0^\infty r^2 Q_{abs} n(r) dr, \tag{2}$$

where

$$Q_{ext} = 2 - 4e^{-\rho tg\beta} \frac{\cos\beta}{\rho} \sin(\rho - \beta) - 4e^{-\rho tg\beta} \left(\frac{\cos\beta}{\rho}\right)^2 \cos(\rho - 2\beta) + 4\left(\frac{\cos\beta}{\rho}\right)^2 \cos 2\beta, \tag{3}$$

$$Q_{abs} = 1 - \exp(-4\chi k) \tag{4}$$

are the expressions of effectiveness factor of the extinction and absorption of the solar radiation by the clouds (*van de Hulst, 1957; Shifrin 1955*), correspondently. ***n*(*r*)** is cloud particle distribution function, $\rho = 2\chi(m-1)$, $\chi = 2\pi r/\lambda$, $tg\beta = k/(n-1)$, ***r*** is particles radius, λ is wavelength, ***m*** is media refraction index, $m = n - ik$, ***n*** is the real part of the refraction index, ***k*** is the image part of the refraction index .

Two parameters gamma – distribution function is prescribed:

$$n(r) = \frac{N_0}{\Gamma(\alpha+1)\beta^{\alpha+1}} r^\alpha \exp\left(-\frac{r}{\beta}\right) \tag{5}$$

α is assigned as constant, β is variable value that calculated during the humidity model integration.

Using (1) - (5) values of the absorption and extinction coefficients could be calculated.

The cloud optical characteristics were calculated in the dependence of the cloud liquid water content, mean particles radius and the asymmetry parameter of the phase function that is depend upon the effective particles radius according Slingo (*1989*).

The results of calculation of the liquid cloud albedo and transmission are presented on Fig. 1. and Fig. 2.

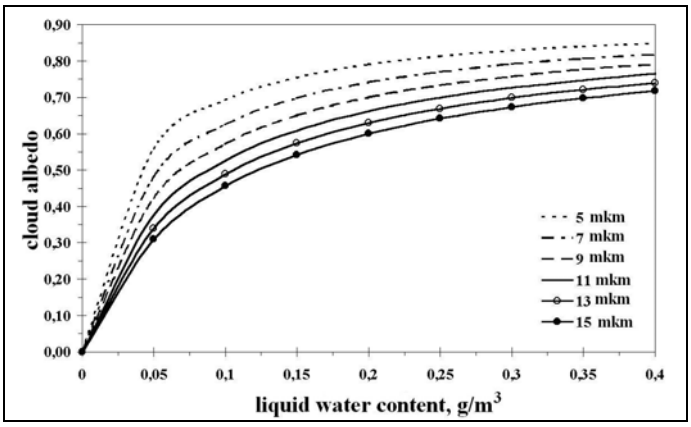

Fig. 1. Cloud albedo in dependence of liquid water content and mean particles radius

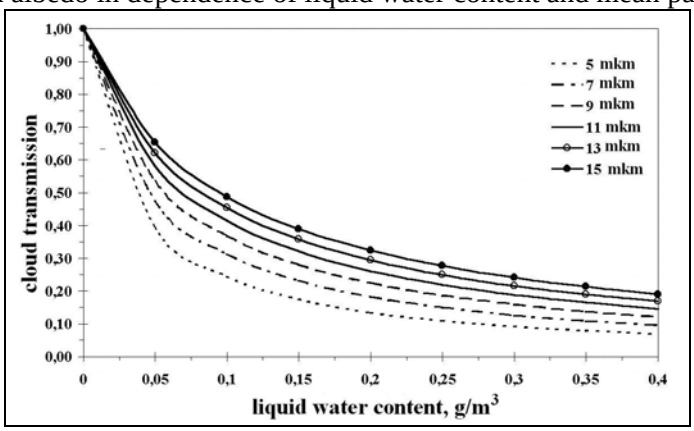

Fig. 2. Cloud transmission in dependence of liquid water content and mean particles radius

As follows from the Fig. 1 cloud albedo is depends at the first upon the liquid water content. The maximum difference in albedo is near 30-40% under the mean radius variation within the limits of 5-15 mkm and liquid water content variation from 0,05 to 0,1 g/m^3. The variation of the transmission (Fig. 2) with in the same interval of liquid water content may be two times more. The more the mean particles radius, the greater the transmission value.

The presented algorithm may be used in the hydrodynamical model of the atmosphere that includes the cloud water content transfer equations.

References:

Dmitirieva-Arrago L.R, Shatunova M.V., 2001: Investigation of the dependence of solar radiation characteristics of the atmosphere on atmosphere, cloud and underlying surface properties. SPIE Proceedings "Atmospheric and ocean optics. Atmospheric physics", 4678

Dmitrieva-Arrago L.R., 2004a: The methods of short-term forecast of the nonconvective clouds and precipitation on the basis of the humidity transformation model with microphysics parameterization. Part 1. Humidity transformation model in the atmosphere and forecast of the noncovective cloudiness.

Dmitrieva-Arrago L.R., 2004b: The methods of short-term forecast of the nonconvective clouds and precipitation on the basis of the humidity transformation model with microphysics parameterization Part 2. The method of the precipitation forecast based on the calculated fields of the liquid water content and parameterization of the microphysical processes in noncovective clouds.

van de Hulst, 1957: Light scattering by small particle. New York, J.Wiley & Sons, Inc.

Shifrin K.S., 1955: To the cloud radiative properties calculation. MGO proceeding, 46(108)

Slingo, A., 1989: A GCM parameterization for the shortwave radiative properties of the water clouds. J.Atmos.Sci., 46

A PDF-based method for computing the sedimentation effects within a full prognostic microphysical scheme

Jean-François Geleyn, Czech Hydrometeorological Institute, Prague, Czech Republic (*)
Yves Bouteloup, CNRM-GMAP, Météo-France, Toulouse, France
Bart Catry, Ghent University, Ghent, Belgium
Radmila Brožková, Czech Hydrometeorological Institute, Prague, Czech Republic
(*) on leave of absence from Météo-France / email: jean-francois.geleyn@chmi.cz

Motivation: When performing cloud and precipitation microphysical computations in a system where all hydrometeors are prognostic, including thus the local quantities of precipitating drops or flakes, the problem arises on how to account for the differences in vertical velocity between those falling species and the total mass of the atmospheric particle. The difficulty is not so much the differential downwards vertical advection of drops/flakes in itself, but the need to treat in a physically-sound way its interactions 'along the trajectory' with other significant microphysical processes (auto-conversion, collection, evaporation-melting, to name only the main ones). To our knowledge, all solutions proposed up to now for solving this complex problem rely on an algorithmic interlacing between dynamical-like advection steps and locally treated microphysics equations. The advection steps may be of the Eulerian type (in which case a time-iterative procedure is needed to avoid violating the CFL condition) or of Lagrangian type (in which case the iterative part of the computation consists in double vertical loops twinning the 'passing by' drops/flakes with the local properties determining auto-conversion, collection, …). In any case these methods are rather expensive. The purpose of this note is to propose a radically differing approach to the problem, which shall eliminate the need to do iterative computations while keeping a high level of accuracy, thanks to the use of a probability distribution function (PDF) framework.

Method:
One may look at the above problem from the angle that advective methods require a unique (mean) fall speed ($\boldsymbol{w_0}$) for any type of precipitating hydrometeor. Let one however assume that this is replaced by a spectrum of fall speeds going from zero to infinity, $\boldsymbol{w_0}$ now being the mass weighted average $\boldsymbol{w}$ for this spectrum. For a given time interval (the model's time step in any concrete application) this spectrum may easily be converted into one of 'reachable distances along the vertical'. At that stage one is apparently in an even worse situation than previously, with an infinity of trajectories to handle. But one may go one step further and convert mathematically (with some hypotheses, see below) the 'distance-related spectrum' into a probability of leaving a given part of the atmospheric slab (down to the bottom of the considered model layer in any concrete application).

Starting from a basic PDF $\boldsymbol{P_0}$, for the probability of one steadily falling hydrometeor to cross the considered layer within one time step, one needs at the bottom of this layer three 'effective' PDFs for falling species:

- Already present in the layer at the beginning of the time step [PDF $\boldsymbol{P_1}$];
- Coming from the layer above [PDF $\boldsymbol{P_2}$];
- Locally produced during the time-step by auto-conversion, collection and melting (or destroyed by evaporation and melting) [PDF $\boldsymbol{P_3}$].

In principle, the various steps leading to these three functions are only meaningful if the resulting implicit local PDFs at the bottom of one given layer are homothetic so that they may be recombined into a single 'entering PDF' at the top of the next layer below. This property

can only be warranted if the $\boldsymbol{P_0}$ function is of the decreasing exponential type, e.g. $P_0(Z) = \exp(-Z) = \exp(-\delta z/(w_0\,\delta t))$, with $\boldsymbol{Z}$ a kind of inverse mean Courant number for the sedimentation process.

It is however our practical experience that starting directly from $\boldsymbol{P_1}$, $\boldsymbol{P_2}$ and $\boldsymbol{P_3}$ functions (without homothetic shape assumption) can also provide good results, provided their derivation obeys some logic, for instance that of mimicking a Lagrangian sedimentation scheme.

For a given $\boldsymbol{P_0}$, while the choice of $\boldsymbol{P_1}$ is in principle straightforward (it should be the average of $\boldsymbol{P_0}$ for a vertical range varying from zero to the full layer's depth), the choices for $\boldsymbol{P_2}$ and $\boldsymbol{P_3}$ must take into account the time dimension within the time-step. Hence their choice may ultimately depend on the way one wishes the various microphysical processes to interact (sequentially or in parallel; with a stationary target for an implicit discretisation or not; etc.). It is out of the scope of this note to deal with this issue, but some care is of course needed to make the choices of $\boldsymbol{P_2}$ and $\boldsymbol{P_3}$ compatible with the other underlying hypotheses of the microphysical scheme.

Remarks:

- The mathematical similarity (in the choice of $\boldsymbol{P_0}$) with the Marshall-Palmer (M-P) law indicates a correct physical behaviour (there are more small drops likely to stay in one layer than big ones that shall anyhow leave it) but it should not be misinterpreted as an identity. In the M-P case it is the slope of the distribution that varies with rain intensity, here it is the total number of drops, in first approximation.
- In principle, the mean fall speed should stay constant when going from one layer to the next one below. But the heuristic approach to make $\boldsymbol{w_0}$ depend on the precipitation intensity (alike in nature) works fine, contrary to the advective case where it would be a likely source of numerical noise. But this does not identify our basic PDF with the M-P law; it just makes it a little bit closer in practice. Note however that both functions need the existence of a 'deus ex machina' process within the complexity of the full microphysical computations in order to see their shapes preserved.
- The concrete application of the method advocated here is strongly related to the tendency ⇔ flux divergence framework of the Green-Ostrogradsky theorem. For instance it allows a direct insertion of any microphysical 'local' computation within the flux-conservative equation framework of Catry et al. (2007).
- When using infinite fall speeds, the above scheme automatically degenerates into a 'classical' diagnostic scheme for precipitating species, whatever may be the handling of non-sedimentation microphysical processes.

Results: After successful pre-operational tests, the scheme presented here was introduced in the ALADIN-CE operational NWP application at CHMI (Prague) on 30/1/07. The set-up uses the decreasing exponential choice for $\boldsymbol{P_0}$, something that may take the name of 'statistical sedimentation scheme', and relies on a sequential split-implicit treatment of microphysical processes. The same version of the scheme is under trial in the services of several ALADIN partners, with promising results. At Météo-France, a version mimicking the operational Lagrangian sedimentation treatment and using an interactive microphysical algorithm is undergoing parallel tests, with a view to obtain operationally unchanged meteorological results, but at a significantly reduced computing cost.

Catry, B., J.-F. Geleyn, M. Tudor, P. Bénard and A. Trojakova, 2007. *Tellus A*, **59**, pp. 71-79.

Implementation of improved Mellor-Yamada Level 3 scheme and partial condensation scheme to JMANHM and their performance

Tabito Hara

Numerical Prediction Division, Japan Meteorological Agency,
1-3-4, Otemachi, Chiyoda-ku, Tokyo 100-8122, Japan
E-mail: tabito.hara@met.kishou.go.jp

1 Introduction

JMANHM is a non-hydrostatic model which is being developed in the Japan Meteorological Agency(JMA). It is employed as an operational mesoscale model (MSM) for 15-hour forecast 8 times a day to provide information for preventing disaster such as severe rain, wind and so on[1].

The horizontal resolution of MSM was enhanced from 10 km to 5km in March 2006, and we plan to expand forecast time of MSM from 15 hours to 33 hours in May 2007. At the same time, the model of which many physical processes are improved will be in operational[2]. One of the improvements is the turbulence scheme which is a main topic of this report.

It has been pointed out that diurnal changes of surface temperature and wind speed predicted by the current MSM are small, that is, it has the negative bias in the daytime and the positive bias in the nighttime. It is possibly caused by the inappropriate representation for transportation of momentum and heat by turbulence in the boundary layer and the insufficiency of short wave radiation flux to surface due to excessive cloud fraction diagnosed by relative humidity.

To get improved for the problem, the improved Mellor-Yamada Level 3 scheme (MY3)[3][4][5] is introduced to JMANHM. Furthermore, cloud fraction and cloud water content used in the radiation process are calculated by the partial condensation scheme[6] with outputs from MY3.

It is confirmed that the model with the improved MY3 and the partial condensation scheme is better on diurnal changes of surface temperature and wind speed and vertical profiles of temperature and wind through our experiments. They will be adopted in the next operational model scheduled in May 2007.

In this report, we will introduce the implementation of MY3 and partial condensation schemes to JMANHM and their performances.

2 Turbulence scheme and cloud in the radiation process of the current MSM

The turbulence scheme of the current MSM is based on Klemp and Wilhelmson[7], in which the coefficients of diffusion which determine the physical quantities of transportation depends on turbulence kinematic energy (TKE) and mixing length. The algebraic equation to get TKE is derived by forecast equation for TKE by neglecting terms of time differential, advection and diffusion of itself assuming the balance between local producing and dissipation of TKE, and TKE is calculated diagnostically by solving the algebraic equation. To consider non-local effect, mixing length is estimated dependently on the height of boundary layer according to Sun and Chang[8]. Because of diagnostic scheme to calculate TKE, the variation of TKE at each time step is considerably large and it possibly disturbs the atmospheric field in the model. Moreover, the mixing length seems not to be suitable in many cases. In some cases it is excessively long and boundary layer is destroyed as a result.

On the other hand, short wave radiation flux in the current model is much less than that of observation because of too much cloud fraction by diagnosis with relative humidity[9]. It is tried to use the quantities of the cloud microphysics in the radiation process, but the coverage of cloud is too small and consequently too large short wave radiation flux pours on surface. It is because cloud water and cloud ice in the cloud microphysics are produced only at saturated grid, and it suggests necessity to introduce the scheme in which cloud water can be produced even if it is not saturated.

3 Introduction of the improved Mellor-Yamada Level 3 scheme and the partial condensation schemes

Mellor-Yamada scheme is the second-order turbulent closure model. In its Level 3 scheme, the variables to be forecasted are TKE, $\theta_l'^2$, $q_w'^2$, $\theta_l' q_w'$, where θ_l', q_w' are the fluctuations from the average values of liquid water potential temperature and total water content respectively. The counter-gradient terms which are considered as non-local effect are naturally appeared as correction of the coefficients of diffusion.

In the improved Mellor-Yamada Level 3 scheme, closure constants and mixing length are corrected based on large-eddy simulation (LES). Stabilization for integrating forecast variables is also taken.

The partial condensation scheme gives cloud fractions and cloud water content through a probability density function (PDF) on θ_l', q_w', which we assume bi-normal distribution. The attributes of PDF determine how much vapor partially condensates at an unsaturated grid. The width σ of distribution function depends on θ'^2, $q_w'^2$, $\theta_l' q_w'$. The evaluated cloud fraction and cloud water content are applied in the radiation process and the turbulence process.

We are provided source code of the main part of the improved MY3 and the partial condensation scheme by Dr. Nakanishi who is the developer of the improved MY3, and we implemented it to JMANHM with some changes.

We add the further improvement as following:

- While total water content q_w consists of mixing ratio of vapor q_v and cloud water q_c in the original code, mixing ratio of cloud ice q_i is additionally considered. Condensed water q_l is assigned to q_c more than 0°C, q_i under -36°C, and q_c and q_i linearly on a temperature between 0°C and -36°C.
- Not only turbulence contributes to produce subgrid cloud, but also cumulus convection and so on. The width of PDF σ is limited to a minimum value which depends on saturated vapor amount to consider the effect. It means that production

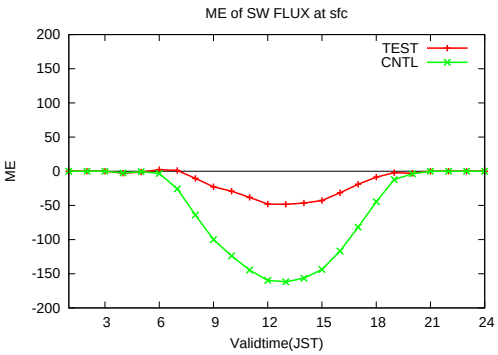

Fig. 1: Mean error of short wave radiation flux in models compared with observations for each local time. Unit: W/m^2. Green line: the current MSM. Red line: the new MSM which includes the improved MY3 and the partial condensation schemes.

of cloud water becomes easier than without this limitation.

4 Performance

The statistical verifications for the new MSM including the improved MY3 and the partial condensation scheme are displayed on [2]. The more realistic diurnal changes of surface temperature and wind velocity and more accurate vertical profiles of temperature and wind are brought mainly by the adoption of these schemes. (It is found through our experiments for impact of each improved physical process that the other improvements do not contribute to these improvements very much.)

Fig.1 shows the comparison of short wave radiation flux to surface between model and observation. While the flux of the current model (green line) has large negative bias, that of the model with those new schemes (red line) is well reduced.

Fig.2 shows the impact of introducing the improved MY3 and the partial condensation scheme for precipitation forecasts. Although the position of rainband differs from the corresponding observation, the rainband is forecasted clearer by the model with those schemes. In this case, because the transportation of momentum from upper to lower is larger than the original model, wind velocity becomes faster and convergence at lower layer seems to be strengthened.

5 Conclusion and Remarks

The improved Mellor-Yamada Level 3 and the partial condensation scheme works much better on diurnal changes of surface temperature and wind, vertical profiles of temperature and wind. And it gives remarkable impact for a heavy rain case. They are included in the new MSM which will operationally run in May 2007.

In the partial condensation scheme, condensed water is used only in the radiation process and the turbulence process, in which buoyancy flux is evaluated, and does not affect the variables in the cloud microphysics. Because cloud water should not exist on unsaturated grid in the current cloud microphysics scheme, inconsistency occurs if the partial condensation is allowed. (For example, partially condensed water evaporates soon.) It is our future work that how the cloud microphysics and the partial condensation scheme can be consistently combined.

References

[1] K.Aranami and T.Segawa. Verification of mesoscale forecasts by a high resolution non-hydrostatic model at jma. *CAS/JSC WGNE Res. Activ. Atmos. Oceanic Modell.*, 36, 66–67, 2006.

[2] T.Hara, K.Aranami, R.Nagasawa, M.Narita, T.Segawa, D.Miura, Y.Honda, H.Nakayama, and K.Takenouchi. Upgrade of non-hydrostatic operational mesoscale model at jma. *CAS/JSC WGNE Res. Activ. Atmos. Oceanic Modell.*, 37, 2007.

[3] M.Nakanishi. Improvement of the mellor-yamada turbulence closure model based on large-eddy simulation data. *Bound.-Layer Meteor.*, 99, 349–378, 2001.

[4] M. Nakanishi and H. Niino. An improved mellor-yamada level 3 model with condensation physics : Its design and verification. *Bound.-Layer Meteor.*, 112, 1–31, 2004.

[5] M. Nakanishi and H. Niino. An improved mellor-yamada level-3 model: Its numerical stability and application to a regional prediction of advection fog. *Bound.-Layer Meteor.*, 119, 397–407, 2006.

[6] G. Sommeria and J.W. Deardorff. Subgrid-scale condensation in models of nonprecipitating clouds. *J. Atmos. Sci*, 34, 344–355, 1976.

[7] J.B. Klemp and R.B. Wilhelmson. The simulation of three-dimensional convective storm dynamics. *J.Atmos.Sci.*, 35, 1070–1096, 1978.

[8] W. Y. Sun and C. Z. Chang. Diffusion model for a convective layer. part i: Numerical simulation of convective boundary layer. *J. Climate Appl. Meteor.*, 25, 1445–1453, 1986.

[9] R.Nagasawa. Improvement of a radiation process for the non-hydrostatic model. In *12th Conference on Atmospheric Radiation*, pages P2–10. American Meteorological Society, 2006.

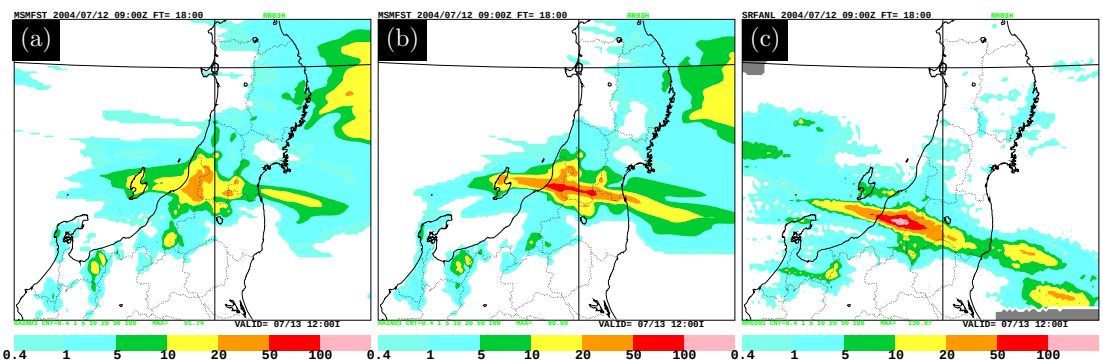

Fig. 2: Forecasted 3-h precipitation (unit: mm) at forecast time 18 hours with the initial time of 09UTC 12 July 2004. (a) the current MSM. (b) MSM with the improved MY3 and the partial condensation scheme. (c) corresponding observation.

Cloud processes simulated by the Canadian Regional Climate Model along a cross-section in the Pacific Ocean

Yanjun Jiao and Colin Jones

Department of Earth and Atmospheric Sciences
University of Quebec at Montreal, Montreal, Quebec, Canada
email: jiao.yanjun@uqam.ca and jones.colin@uqam.ca

In this study, the 4th generation of the Canadian Regional Climate Model (CRCM) has been integrated over the Pacific Ocean in the context of the GCSS (GEWEX Cloud System Study) Pacific Cross-section Intercomparison (GPCI), which is an international project to evaluate and improve the representation of cloud and precipitation processes in weather and climate prediction models.

The CRCM was run at 180-km resolution over the Pacific Ocean with 115x75 grid points in the polar stereographic projection (Fig.1). Instantaneous model results are output every 3 hours for the periods of June-July-August (JJA) 1998. Seasonal mean results simulated by the CRCM are analyzed and compared with different observations and reanalysis data along a cross-section in the Pacific Ocean, which extends from the stratocumulus regions off the coast of California, across the shallow cumulus areas in the central Pacific Ocean, down to the deep convection regions of the ITCZ.

A number of modifications have been introduced in the model physics in order to improve the simulation of the cloud properties in the CRCM. The modifications are briefly summarized as:

1. A switch has been added to turn off the shallow convection once the deep convection had been detected on the same grid point.

2. A temperature perturbation based on the mean relative humidity in the mixing layer has been added in the trigger function of shallow convection; and the free convective vertical velocity scale been used in the cloud base mass flux closure of the shallow convection.

3. In the deep convection, cloud radius and the minimum cloud-depth threshold have been updated according to Kain (2004) rather than remaining constants. A dilute updraft ascent has been used to calculate convective available potential energy (CAPE) in the closure, which provides a more accurate calculation in convection rainfall and mass flux.

4. The calculation of the eddy diffusivities has been upgraded based on the scheme from the ECMWF; the entrainment at the top of boundary layer has been considered based on Grenier and Bretherton (2001).

5. The large-scale cloud fraction has been diagnosed following Xu and Randall (1996).

6. The evaporation of the falling larger scale precipitation has also been considered.

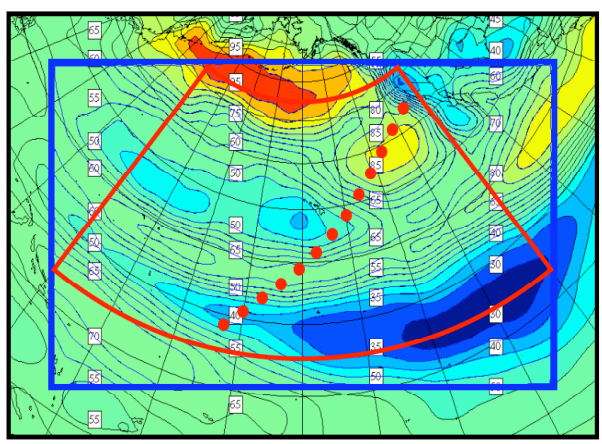

Fig.1. CRCM computational domain in the polar stereographic projection. The blue line is the sponge zone of the model; the dotted line indicates the location of the cross-section; the solid red line represent the 2-dimentional common area required by the GPCI. The contours are observed seasonal mean cloud cover from ISCCP for JJA 1998.

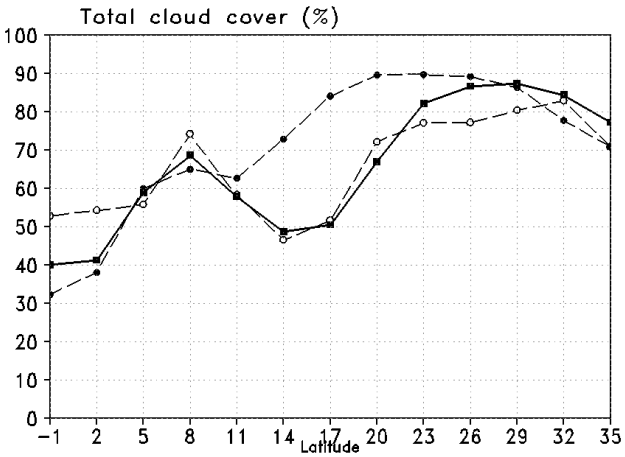

Fig.2. Seasonal mean total cloud cover simulated by the modified CRCM (dashed line with circles), the original CRCM (dashed line with dotes) and the observation from ISCCP (solid line) along the GPCI cross-section for the period of JJA 1998.

Comparison results show that these modifications have a significant beneficial influence on the CRCM simulation. Great improvements have been found in the simulated total cloud cover over the shallow convective region (Fig. 2) while comparing with the observation form the International Satellite Cloud Climatology Project (ISCCP). Some improvement in the fields of simulated vertical structure of the relative humidity (Fig. 3), cloud distribution and vertical velocity have also been noticed while comparing with the ERA40 reanalysis.

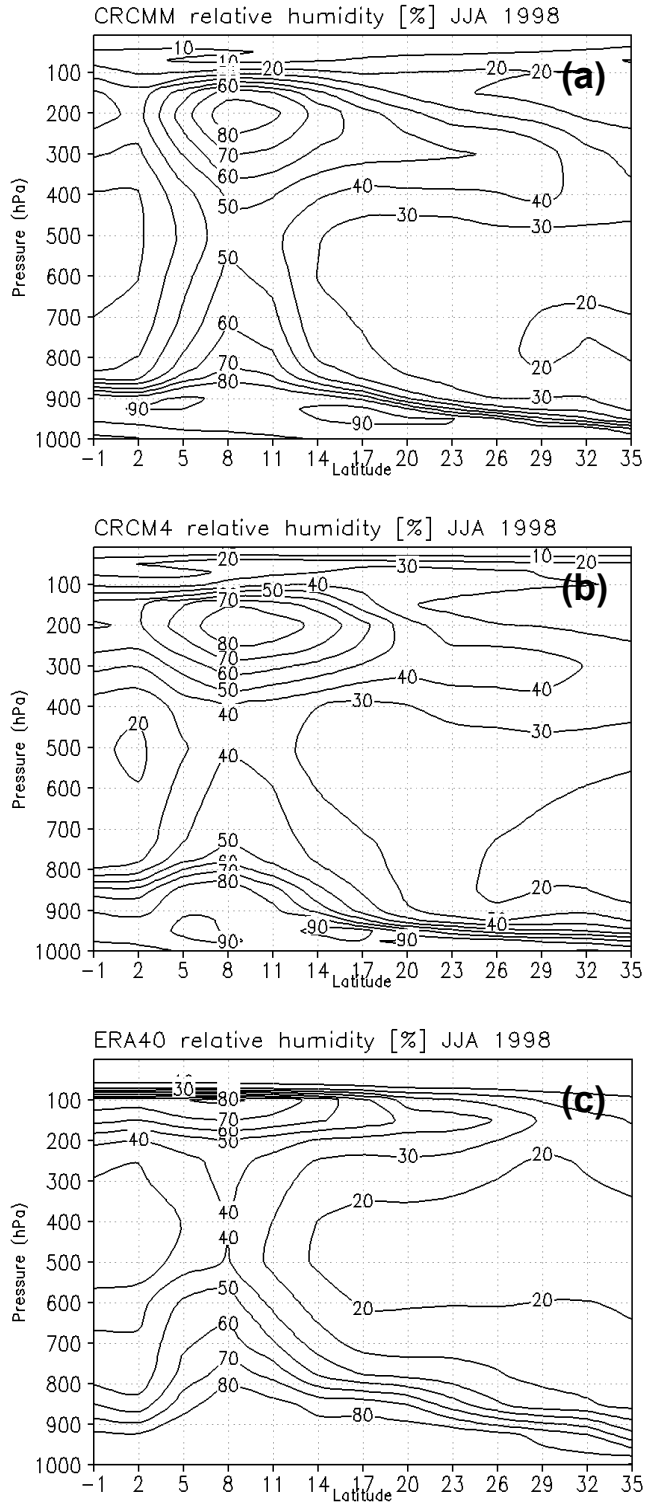

Fig.3. Vertical structures of the seasonal mean relative humidity simulated by (a) the modified CRCM, (b) the original CRCM, and (c) the ERA40 reanalysis along the GPCI cross-section.

References:

Grenier, H., and C. S. Bretherton, 2001: A moist PBL parameterization for large-scale models and its application to subtropical cloud-topped marine boundary layers. Mon. Wea. Rev., **129**, 357–377.

Kain, J. S., 2004: The Kain–Fritsch convective parameterization: An update. J. Appl. Meteor., **43**, 170–181.

Xu, K.-M. and D. A. Randall, 1996: A semiempirical cloudiness parameterization for use in climate models. J. Atmos. Sci., **53**, 3084-3102.

WRF-ARW sensitivity to different planetary boundary layer parameterization over South America

Juan Ruiz, Ferreira Lorena and Celeste Saulo
Centro de Investigaciones del Mar y la Atmósfera, Departamento de Ciencias de la Atmósfera y los Océanos, Facultad de Ciencias Exactas y Naturales, Universidad de Buenos Aires.
jruiz@cima.fcen.uba.ar

1. Introduction:

The WRF-ARW (Advanced Research- Weather Research and Forecasting) model has been implemented at CIMA (Centro de Investigaciones del Mar y la Atmósfera) since November 2005, to provide operative short range, mesoscale weather forecasts over South America (http://wrf.cima.fcen.uba.ar). Since then, some studies (Ruiz and Saulo, 2006) have been devoted to evaluate WRF performance over South America since there is almost no documentation about its performance over this particular region

Preliminary analysis of these operational forecasts, show that forecasted surface temperatures are lower than the observed values. This systematic bias could be caused by several reasons, e.g. misrepresentation of heat fluxes at the surface or limitations in the Planetary Boundary Layer parameterization (PBL). In order to address the deficiencies in the representation of temperature at low levels, we report here the results obtained from the analysis of model sensitivity to the use of two different planetary boundary layer (PBL) parameterizations, which are provided with the WRF-ARW code.

2. Methodology:

The experimental design for this study consists of the following:

1) Experiment 1: In order to assess the impact of alternate PBL parameterizations, two series of 48 hr-forecasts were performed between October 22nd and November 27th 2005, initializing the model at 12 UTC and using the Global Forecasting System to obtain initial and boundary conditions. One of the series runs with the Yon Sei University PBL scheme and the other with Mellor, Yamada and Janjic scheme (Mellor and Yamada, 1982). All other model settings were kept identical between the series. The horizontal resolution is 50 km with 31 sigma vertical levels.
2) Experiment 2: In order to compare model forecasts with high resolution observations available from the South American Low Level Jet Experiment field campaign, two ten day-simulations were performed using the same PBL schemes as in the previous experiment. These runs have 20 km resolution and start on 29th January 2003 with GDAS (Global Data Assimilation System) analysis used to provide both, initial and boundary conditions. This case corresponds to a Norwesthern Argentinian Low (NAL) event which is a thermal-orographic low pressure system (see Seluchi et. al., 2003 for a description of the NAL). The thermal component of this system makes it very sensible to heating at low levels. In this work, radiosounding observations performed at Santiago del Estero (27ºS, 64ºW see Figure 1 a for station location) are used to test model performance with emphasis on the diurnal cycle of the PBL structure at 06 and 18 UTC.

3. Results:

Fig. 1 a and b, show the averaged difference (over the experimental period) of 2 meter temperature at 06 and 18 UTC for experiment 1. In general it can be seen that the YSU scheme gives temperatures greater than the MYJ at both times of the day. During the warm hour, differences are larger (greater than 1.5K) and cover most of the domain. At 06 UTC, maximum differences can be found over La Plata Basin and over areas with relatively low terrain height. Fig. 1 c and d, show the difference in wind and moisture convergence at 850 hPa.. The difference wind field resembles the climatological circulation at low levels but running in the opossite direction. This suggests that the circulation associated with the "trade winds-low level jet-SACZ" patterns over South America is stronger when the model uses MYJ PBL parameterization. Differences in wind and moisture fields lead to changes in the distribution of moisture convergence (Fig 1 c and d) as can be seen over eastern Brazil, where the MYJ scheme produces stronger low level moisture convergence. This migth have an impact in the distribution of precipitation. However, the relation between changes in moisture convergence and precipitation is not as close as it could be expected (not shown).

Fig. 2 a, b and c, show a height–time cross section of the observed potential temperature at Santiago del Estero and the differences between the observed and the forecasted potential temperature for the Experiment 2. During warm hours a well mixed layer develops, reaching 750hPa and denoting an intense warming during most of the period. Both schemes (Fig. 2 b and c) underestimate the observed potential temperature although YSU temperatures are warmer than MYJ ones, in agreement with experiment 1 results. As in Fig. 1 a and b, potential temperature differences among both schemes are greater during the warm hour, when the NAL is more intense. Similar results were obtained for Resistencia (27.5ºS 59.0ºW) upper air observations available at the same UTC times during the experimental period (not shown).

To analyze the potential impact of the PBL parameterization upon a this low pressure system, the observed sea level pressure series at La Rioja station (29°S, 66°W), which is collocated with the NAL center, is compared with the forecasted values using the two PBL schemes (Fig. 2 d). As can be seen, both simulations retain the observed pressure evolution but underestimate the deepening of the NAL. YSU shows a slightly better performance, what might be related to the warmer PBL associated with this scheme.

Acknowledgments: *This research is sponsored by the Research Grants UBACyt X155 and CONICET PIP 5417.*

References

Ruiz, J., A. C. Saulo and Eugenia Kalnay: **A regional ensemble forecast system for southeastern south america: preliminary assessment.** *Proceedings of 8 ICSHMO*, Foz do Iguazu, Brazil, April 24-28, INPE, p. 1977-1984.

Saulo A.C., Ferreira L., Mejia J. and Seluchi M.,2004**: Description of the Termal Low Characteristic using SALLJEX Special Observations**. *Clivar Exchanges*, 9, 9-10 y 17

Seluchi, M., A.C. Saulo, M. Nicolini, y P. Satyamurty, 2003: **The Northwestern Argentinean Low: A Study of Two Typical Events**. *Mon. Wea. Rev.*, Vol 131, 2361-2378.

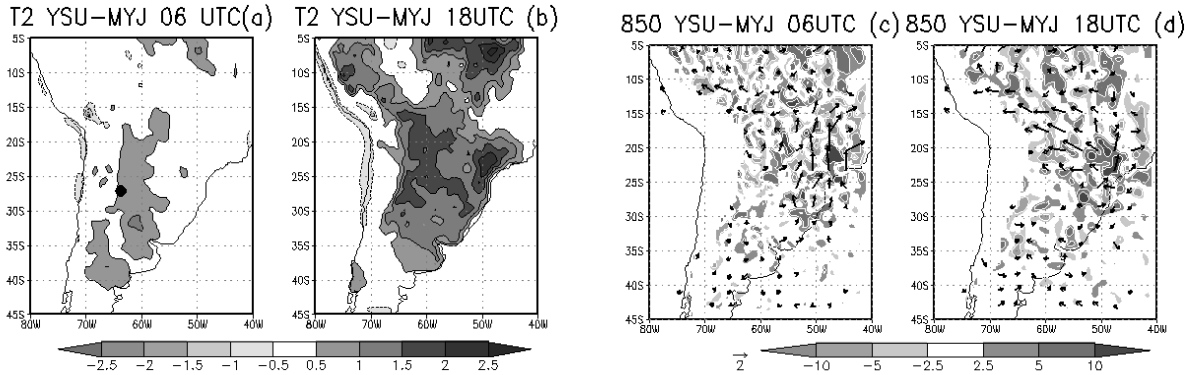

Figure 1: (a) and (b) Differences between temperatures at 2 meters (YSU-MYJ) at 06 and 18 UTC respectively. (c) and (d) 850 hPa. wind differences (YSU-MYJ) (vectors) (only values above 2 ms^{-1} are plotted) and moisture convergence differences (YSU-MYJ) (10^{-8}g kg^{-1} m s^{-1}) (shaded). The black dot in figure (a) shows the location of Santiago del Estero.

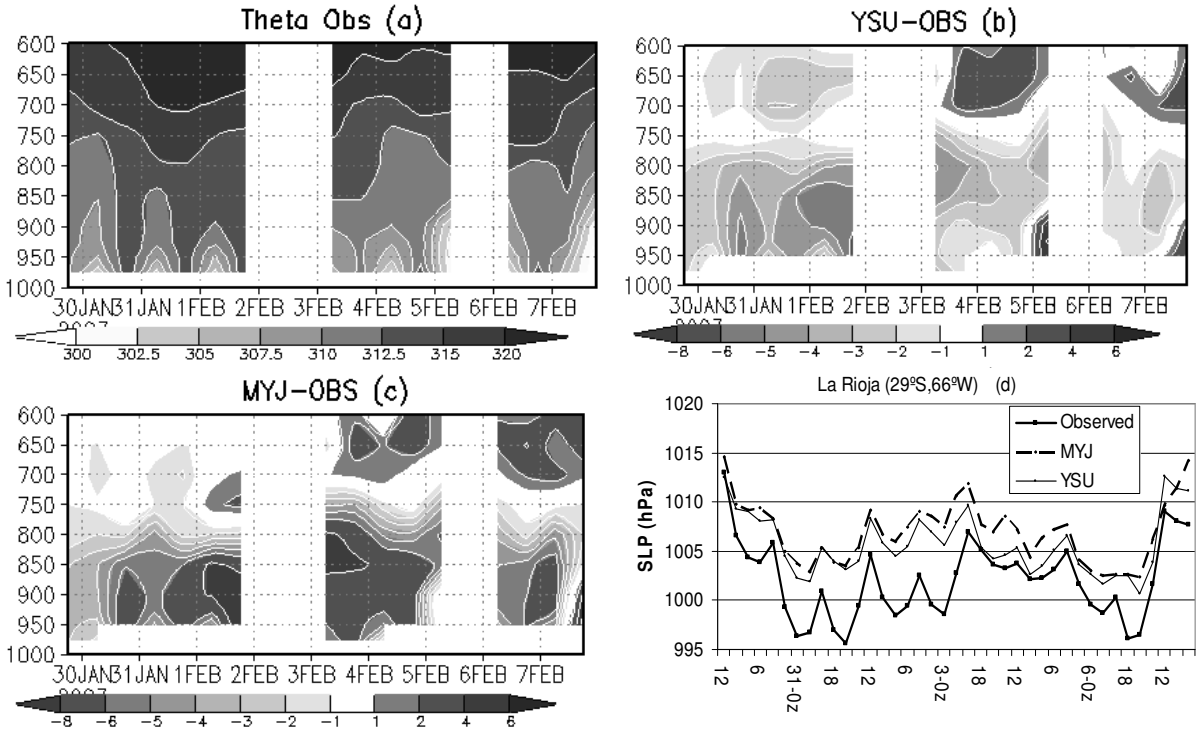

Figure 2: Height-time cross section of (a) observed potential temperature (in K) (b) YSU minus observed potential temperature and (c) MYJ minus observed potential temperature at Santiago del Estero. (d) Observed pressure evolution at La Rioja (solid thick line), YSU PBL forecast (solid thin line) and MYJ PBL forecast (dashed line) . All figures are for experiment 2 between 29th January 2003 and 08th January 2003.

The Impact of the Sea State on the Typhoon Intensity in Atmosphere-wave coupled model

Nadao Kohno and Akihiko Murata
Meteorological Research Institute, JMA Tsukuba, Ibaraki 305-0052, Japan
E-mail: nkohno@mri-jma.go.jp

1. Introduction

It is necessary to estimate accurately the amount of momentum and heat exchanges, for evaluating the correct typhoon intensity. Especially, very rough sea condition under a typhoon, where high ocean waves are generated by storm wind and many sea sprays are flying, air-sea interaction is supposed to be influenced by the sea state (ocean waves).

However the flux dependency on sea state has not been solved satisfactorily yet, even though this knowledge shall give the important basis about the coupling mechanism between the ocean and the atmosphere. Recently several researches have been carried out with an integrated model (e.g. an atmosphere-ocean-wave coupled model), though the fundamental mechanism, how much impact will be given to a typhoon by including the wave dependency on flux, is seldom investigated intensively. Therefore, the impact on typhoon and wave intensity as a joint system with a atmosphere-wave coupled model is investigated, though there is still an uncertainty about the wave dependency itself.

2. Numerical Methods

The numerical model in our calculation is an atmosphere-wave coupled model: the atmospheric model Non-Hydrostatic Model (NHM) of the Meteorological Research Institute / Numerical Prediction Division of JMA (Saito et al., 2001) is coupled with the third generation wave model MRI-III (Ueno and Kohno, 2004). We define the horizontal grid scale as 5km in our calculation, and the NHM has 50 layers in vertical. The wave spectrum consists of 900 components; 25 in frequency and 36 in direction. The frequency of wave spectrum is divided logarithmically from 0.0375Hz to 0.3000Hz.

Since there are various formulae of roughness expression with wave dependency, we checked the performance by three characteristic types, (1) wave induced stress by Janssen (1989), (2) wave age by Smith et al. (1991), and (3) wave steepness by Taylor and Yelland (2001), and the results are inter-compared.

The simulated case is the developing stage of Typhoon Chaba (0416) during 03UTC on Aug 21 2004 to 00UTC on Aug 24. This typhoon slowly moved west and developed to a large and strong typhoon, the central pressure felled down to 910hPa from 985hPa in this period (69hours).

3. Calculation Results

Figure 1 depicts the scatter plot of C_d and U_{10}. The upper left is calculated by the formula of Kondo (1975), which has only wind dependency and used in standard NHM. It is easily recognized that the drag coefficients with wave dependency have large values in general. C_d values tend to be large in the strong wind, though C_d scatter is rather apparent in middle wind speed.

This large value decreases the lower wind speed as a strong resistance, and the typhoon were retarded to develop. In general, typhoon showed weak development in all

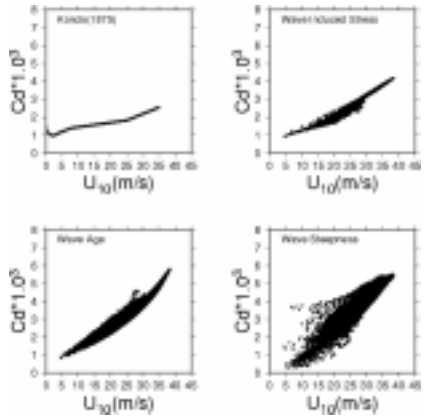

Fig. 1. The calculated drag coefficients

calculations with the coupled model. However, the typhoon showed rapid intensification as the time goes on, and in some case typhoon intensity became rather stronger than that of uncoupled case in the last time. This impact also may come from the large C_d value: The large drag makes inflow in lower level larger by frictional effect. This means the enhancement of frictional convergence, and thus leads to the intensification of the primary circulation of typhoon. The radial wind around the typhoon at 18UTC on Aug 23 is shown in Fig. 2. (The typhoon center is 17.5N, 143.6E and moving westward.) In all cases of coupled calculation, the inflow in lower level is strong especially in the right-hand side of typhoon. The tangential wind speed at the same time is shown in Fig.3, which exhibits that wind speed in the right-hand side of typhoon is strong especially in the calculation with wave induced stress. The wind speed in the left-hand side of typhoon is rather weak, and asymmetry in tangential wind speed around typhoon is enlarged. It is also notable that the maximum wind at 850hPa is shifted inside in the coupled cases. This 'shrunk' typhoon structure seems be due to the enhancement of frictional convergence.

According to our results, the drag coefficients tend to have large values when wave dependency is included. This may leads to two impacts: one is the weakening of lower wind speed by the large drag values, and the other is that shrinking of typhoon size by large frictional convergence. The latter case sometimes led to a stronger typhoon than uncoupled one. This means there may be two opposite effect on typhoon intensity, and we are going to investigate the principal mechanism further.

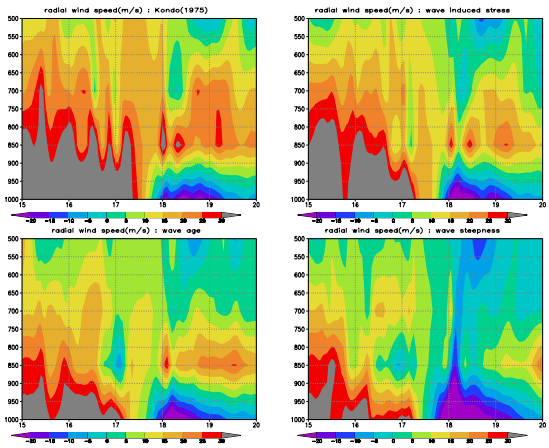

Fig. 2 The radial wind profile (m/s) at 143.6E

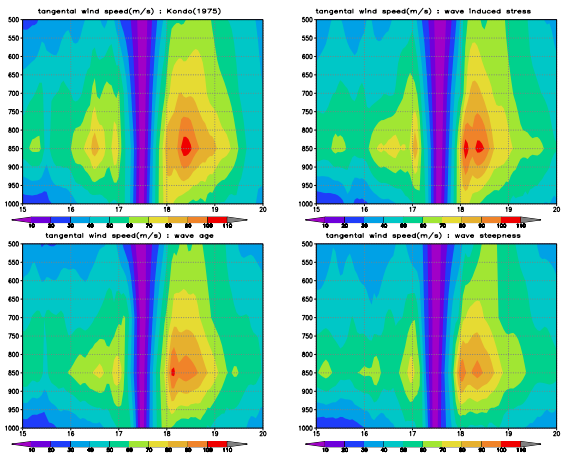

Fig.3 The tangential wind speed (m/s) at 143.4E

REFERENCES

Janssen, P. A. E. M., 1989: Wave-induced stress and the drag of air flow over sea waves. *J. Phys. Oceanogr.*, 19, 745-754.

Kondo, J., 1975: Air-sea bulk transfer coefficients in diabatic conditions. *Boundary-Layer Meteorol*., 9, 91-112.

Saito, K, T. Kato, H. Eito and C. Muroi, 2001: Documentation of the Meteorological Research Institute / Numerical Prediction Division unified nonhydrostatic model. *Tech. Rep. Meteorol. Res. Inst*., 42, 133pp.

Smith, S. D., R. J. Anderson, W. A. Oost, C. Kraan, N. Maat, J. DeCosmo, K. B. Katsaros, K. L. Davidson, K. Bumke, L. Hasse, and H. M. Chadwick, 1992: Sea surface wind stress and drag coefficients: The HEXOS results. *Boundary-Layer Meteorol*., 60, 109-142.

Taylor, P. K. and M. J. Yelland, 2001: The dependence of sea surface roughness on the height and steepness of the waves. *J. Phys. Oceanogr*., 31, 572-590.

Ueno, K. and N. Kohno, 2004: The development of the third generation wave model MRI-III for operational use. *in Proc. 8th Int. Workshop on Wave Hindcasting and Forecasting*, G2, 1-7.

Entrainment and Detrainment in Numerically Simulated Cumulus Clouds and Their Relationship to Buoyancy

Akihiko MURATA

Meteorological Research Institute / Japan Meteorological Agency, Tsukuba, Ibaraki 305-0052, Japan
(corresponding author: amurata@mri-jma.go.jp)

1. Introduction

Entrainment and detrainment in numerically simulated cumulus clouds have been investigated using a cloud-resolving model (CRM) in order to reduce errors induced by cumulus parameterization in coarser-mesh models. Murata and Ueno (2005) investigated the vertical profile of cumulus mass flux using a high-resolution three-dimensional CRM with the 200-m horizontal resolution. They found that the vertical profile of fractional entrainment rate, derived from the calculation based on the vertical gradient of cloud mass flux, have characteristic structures: larger near cloud base and top, and smaller in between (even negative in many cases). The negative values suggest laterally detrained air from a cumulus into the environment. However, it is not clear what factors control the height and amount of detrainment.

In this study, on the basis of the results of the high-resolution CRM simulations, the relationship between detrainment and buoyancy is investigated. We then examine whether buoyancy is useful for determining the height and amount of detrainment in numerically simulated cumulus clouds.

2. Numerical model and experimental design

The numerical model we used was the Japan Meteorological Agency Nonhydrostatic Model (JMANHM; Saito et al., 2006) with the horizontal grid spacing of 200 m (referred to 200 m-NHM). The model was used as a CRM for numerical simulations of cumuli contained in typhoon Songda (2004) just after its genesis. In the numerical simulations, cloud microphysics is explicitly treated and no cumulus parameterization is used. We adopt a grid-nesting strategy for the initial and lateral boundary conditions: quadruple nested JMANHM. Their horizontal grid spacing are 1, 3, 18 km (referred to 1, 3, 18 km-NHM). The initial and lateral boundary data for 18 km-NHM are obtained from forecasts produced by JMA Global Spectral Model (GSM).

3. Detection of entrainment and detrainment

In the analysis of CRM results, assumptions are needed for extracting convective regions from the whole model region. For the extraction, we developed a new method, with which each cumulus area is determined on the basis of convective cores. Some parts of the method followed that proposed by Xu (1995).

For detecting convective cores, the present method uses the horizontal distribution of the maximum cloud updraft strength, Wx, below the melting level, as in the Xu's method. A convective core satisfies one of the following two conditions: 1) Wx > 2Wxa, where Wxa is the average of Wx over the surrounding 24 grid columns, 2) Wx > Wxth, where Wxth = 3.0 ms^{-1}. A cumulus area, in each vertical level, includes a core grid point and other grid points. If the other grid points satisfy the both of the following two conditions, the grid points are assumed to be cumulus grid points. The two conditions are 3) W > Wth, where W is vertical velocity and Wth = 0 ms^{-1}, 4) Qc + Qi > Qth, where Qc and Qi are mixing ratio of cloud water and cloud ice, respectively, and Qth = 0.1 gkg^{-1}.

The entrainment rate calculation was conducted on the basis of the vertical differentiation of updraft velocity as follows: $\partial w/w\partial z$, where w is vertical velocity averaged over a cumulus area and z is height. Positive (negative) values are assumed to represent entrainment (detrainment) in terms of vertical velocity. It should be noted that entrainment rate here is defined on the basis of vertical velocity instead of cloud mass flux because buoyancy does not directly control cloud mass flux but vertical velocity.

4. Relationship between entrainment/detrainment and buoyancy

It is found that favorable heights for detrainment correspond to vertically negative gradient of buoyancy. Figure 1 shows the vertical profiles of vertical velocity and buoyancy in a cumulus area, where buoyancy is defined on the basis of moist air density that includes the effect of water substances. Vertical velocity decreases with height between 5 and 6 km high, indicating that detrainment, in terms of vertical velocity, occurs at those heights. Corresponding to the detrainment, buoyancy decreases with height from 5 to 6 km high.

The correspondence between detrainment and negative buoyancy gradient is observed in many cumulus areas.

The scatter diagram of the relationship between entrainment rate, in terms of vertical velocity, and the vertical gradient of buoyancy is shown in Fig. 2. The diagram for buoyancy instead of the buoyancy gradient is also shown. These figures clearly show the correlation between entrainment rate and the buoyancy gradient rather than buoyancy itself: Positive (negative) buoyancy gradient corresponds to positive (negative) entrainment rate. That is, positive (negative) buoyancy gradient relates to entrainment (detrainment). It should be noted that entrainment rate decreases (i.e., detrainment rate increases) with decreasing the buoyancy gradient. The buoyancy gradient therefore seems to be useful for determining the height and amount of detrainment.

The relationship between the buoyancy gradient and entrainment rate is probably explained by the mechanism proposed by Bretherton and Smolarkiewicz (1989) and Taylor and Baker (1991). They pointed out that the increase of vertical acceleration with height within a cloud brings about a vertical stretch, induces inflow from the environment, and results in enhanced entrainment.

Ackowledgements

The author acknowledges R. Sakai of the Numerical Prediction Division / JMA for supplying the initial data for GSM integration.

References

Bretherton, C. S. and P. K. Smolarkiewicz, 1989: Gravity waves, compensating subsidence and detrainment around cumulus clouds. J. Atmos. Sci., 46, 740-759.

Murata, A. and M. Ueno, 2005: The vertical profile of entrainment rate simulated by a cloud-resolving model and application to a cumulus parameterization. J. Meteor. Soc. Japan, 83, 745-770.

Saito, K., T. Fujita, Y. Yamada, J. Ishida, Y. Kumagai, K. Aranami, S. Ohmori, R. Nagasawa, S. Kumagai, C. Muroi, T. Kato, H. Eito and Y. Yamazaki, 2006: The operational JMA Nonhydrostatic Mesoscale Model. Mon. Wea. Rev., 134, 1266-1298.

Taylor, G. R. and M. B. Baker, 1991: Entrainment and detrainment in cumulus clouds. J. Atmos. Sci., 48, 112-121.

Xu, K.-M., 1995: Partitioning mass, heat, and moisture budgets of explicitly simulated cumulus ensembles into convective and stratiform components. J. Atmos. Sci., 52, 1-23.

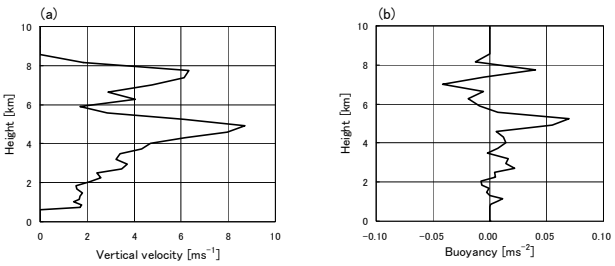

Fig.1 Vertical profiles of (a) vertical velocity and (b) buoyancy, within a cumulus area.

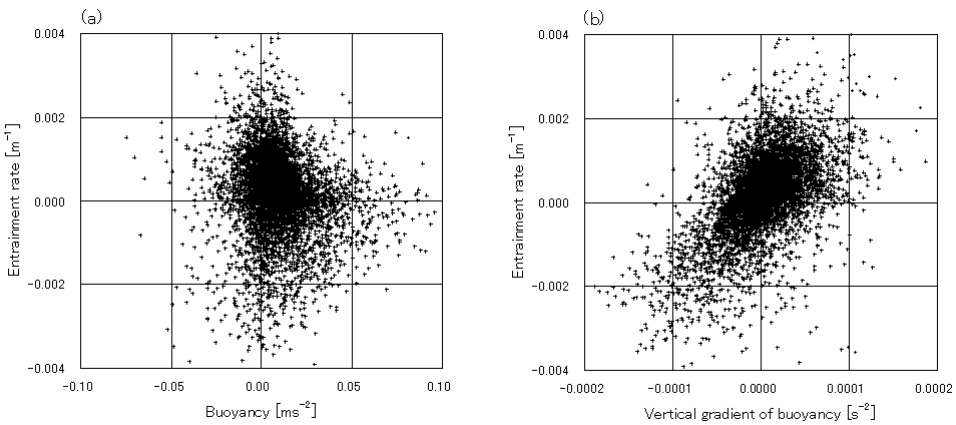

Fig.2 Scatter diagrams of the relationship (a) between buoyancy and entrainment rate, and (b) between the vertical gradient of buoyancy and entrainment rate, within cumulus areas.

Coupled atmosphere-hydrology system for routine prediction of overland water flow

S. Nickovic
ICoD, University of Malta; now at: World Meteorological Organization, Geneva, Switzerland

The atmosphere-soil physical system interacts by exchanging the moisture and heat at their interface. In numerical weather prediction systems, soil parameterization modules provide information on the soil state as a lower boundary condition for atmospheric models. Parameterization of the soil processes includes, among others, columnar water infiltration process. Although the rainfall overland and underground runoff is usual output of the soil parameterization, it is rarely used as a driving parameter for hydrology models. In this study, we describe a system that couples the atmospheric WRF-NCEP/NMM model (Janjic et al., 2001; Janjic, 2002) with a newly developed dynamic hydrology model using the rainfall runoff as a coupling variable.

The NMM model is an advanced nonhydrostatic model developed in the National Centres for Environmental Predictions (NCEP), Washington. The model is introduced in 2006 as the operational regional model, replacing so the hydrostatic Eta model at NCEP. NMM introduces an alternative approach to the design of nonhydrostatic weather prediction models. Instead of extending meso–scale nonhydrostatic modelling concepts to the synoptic scales and beyond, NMM uses a mass based vertical coordinate which has been extended to include the nonhydrostatic motions, preserving so favourable features of the hydrostatic formulation. In order to do so, the system of nonhydrostatic equations was split into two parts: the *first* part that corresponds to the hydrostatic dynamics, and the *second* part that allows computation of corrections due to the nonhydrostatic vertical acceleration. The NMM model 'physics' package is generally the same as used in the Eta model (Janjic 1990, 1994); it includes the Ferrier cloud microphysics, Mellor-Yamada-Janjic turbulence scheme, Betts-Miller-Janjic convection scheme and the GFDL radiation model.

In the NMM model, the NOAH land surface 1-d column model (Chen et al, 1996; Koren et al., 1999; Ek et al., 2003) is applied for the soil processes. NOAH considers both warm-surface and snow-pack/frozen-surface processes. The forcing variables for NOAH are predicted temperature, humidity, wind and surface pressure from NMM. Parameters describing the state of the soil surface are the land cover, soil texture and green vegetation fraction. Four layers (10, 30, 60 and 100 cm thick) are used to describe soil processes. NOAH solves the heat and moisture balance equations at the air-soil interface through direct and canopy water evaporation, water soil infiltration and internal moisture and heat flux processes. In the soil water balance equation, the Richard's equation is applied to simulate the soil water movement. Depending on the soil state, precipitation, evaporation and infiltration, the overland and underground rainfall runoffs are predicted simultaneously with the other atmospheric model variables. Since parameterization of the soil processes includes columnar water infiltration, soil models such as NOAH have a columnar component of the soil hydrology.

This study extends the columnar hydrology process to two other dimensions. For that purpose, we have developed a numerical hydrology prediction model (NHPM) that is designed to use the predicted rainfall runoff from the atmospheric model as a forcing hydrology NHPM solves a full set of shallow-water dynamic equations using a grid point approach. Unlike most of operational hydrology models that simplify the momentum equations to the kinematic (*diagnostic*) form, the NHPM solves all three governing equations (two for velocity components and one for the water height) in the *prognostic* mode. High-resolution data sets for real topography, river routing and land-cover are used to describe the surface physical features. The NHPM '*dynamics'* includes advection, diffusion and water gradient force, while the model '*physics'* (e.g. the friction slope terms) is parameterized, i.e. expressed in terms of the model grid-point variables. NHPM also includes a river-routing sub-model that drives the water excess due to precipitation.

NHPM, being restricted to the surface water dynamics, includes the following major processes: the water movement downhill due to the topography influence; the water movement away from precipitation sources due to the local water surplus and the horizontal water gradients; other components of the water dynamics such as the surface friction, advection and diffusion.

The governing equations are:

$$\frac{\partial u}{\partial t}+u\frac{\partial u}{\partial x}+v\frac{\partial u}{\partial y}+g\left[\frac{\partial h}{\partial x}+S_{fx}-S_{0x}\right]=0 \quad , \quad \frac{\partial v}{\partial t}+u\frac{\partial v}{\partial x}+v\frac{\partial v}{\partial y}+g\left[\frac{\partial h}{\partial y}+S_{fy}-S_{0y}\right]=0 \quad , \quad \frac{\partial h}{\partial t}+\frac{\partial(hu)}{\partial x}+\frac{\partial(hv)}{\partial y}+\dot{H}=0 \quad .$$

Here, $\dot{H}$ is the height source/sink term; $S_{fx}=\frac{n^2\sqrt{u^2+v^2}}{h^{4/3}}u$, $S_{fy}=\frac{n^2\sqrt{u^2+v^2}}{h^{4/3}}v$ are the friction velocity terms; $S_{0x}=-\frac{\partial h_0}{\partial x}$, $S_{0y}=-\frac{\partial h_0}{\partial x}$ are the topography gradient terms; h_0 is the topography height; g is the gravity acceleration; n is the Manning coefficient.

We have developed/applied several numerical methods for the horizontal rectangular semi-staggered grid used in the model (Figure 1). The horizontal advection is represented by a mass conservative, positive definite numerical scheme free of generating new extremes (Janjic, 1997). An explicit forward-backward time differencing scheme for the gravity wave terms (Janjic, 1979) is implemented to provide efficient time integrations of the model.

A new method for mass redistribution at sources/sinks $\dot{H}$ is developed to suppress a computational grid decoupling of gravity waves typical for the semi-staggered grid. The proposed scheme is applied to the continuity equation as:

$$\frac{\partial h}{\partial t} + (\delta_x hu + \delta_y hv) + \frac{1}{2}\left(\dot{H} + \overline{\dot{H}}^{xy} \right) = 0$$

Here, δ_x and δ_y are second-order finite-differencing operators; $\overline{(\ )}^{xy}$ is the averaging operator applied along x and y directions.

Furthermore, a numerical scheme for the friction slope terms based on physical principles is developed. The scheme successfully avoids a singular instability that may occur when vanishing water heights in the denominator of the friction terms generates their uncontrolled growth. The proposed scheme using an implicit time differencing is written in the following form:

$\frac{u^{n+1} - u^n}{\Delta t} + B^n u^{n+1} + g\frac{\partial h_0}{\partial x} = 0$,. Here, $B \equiv \frac{gn^2\sqrt{u^2 + v^2}}{\left(\overline{h}^{xy}\right)^{4/3}}$. The corresponding solution of the scheme is $u^{n+1} = \left[\left(u - g\frac{\partial h_0}{\partial x}\Delta t\right)/(1 + B\Delta t)\right]^n$. Analogous equations are applied to the v velocity component. When the time step Δt vanishes, the velocities at the time level $n+1$ converge to values at the level n, which confirms the numerical consistency of the scheme. Furthermore, when the water depth vanishes, the velocity converges to zero; the stability of the scheme is therefore secured.

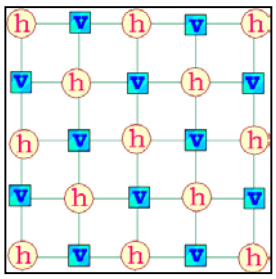

Figure 1. Grid spacing of height and velocity points

NHPM could be easily applied over different geographic domains and be efficiently run on conventional personal computer platforms. Preliminary real-time experiments set up over two smaller watersheds in the Balkan Peninsula have demonstrated that NHPM is capable to successfully simulate major features of the water flood dynamics (Pejanovic, personal communication).

ACKNOWLEDGEMET

Major part of the NHPM developments was performed within the 4th Italo-Maltese Protocol (1995-2000).

REFERENCES

Chen, F., K. Mitchell, J. Schaake, Y. Xue, H.-L. Pan, V. Koren, Q.-Y. Duan, M. Ek, and A. Betts, 1996. Modeling of land-surface evaporation by four schemes and comparison with observations, J. Geophys. Res., 101, No. D3, 7251-7268.

Ek, M. B., K. E. Mitchell, Y. Lin, E. Rogers, P. Grunmann, V. Koren, G. Gayno, and J. D. Tarpley, 2003. Implementation of Noah land-surface model advances in the NCEP operational mesoscale Eta model, J. Geophys., 108, No. D22, 8851, doi:10.1029/2002JD003296, 2003.

Janjic, Z. I., 1979: Forward-backward scheme modified to prevent two-grid-interval noise and its application in sigma coordinate models. *Contributions to Atmospheric Physics,* Vol. **52**, 69-84.

Janjic, Z. I., 1990: The step-mountain coordinate: physical package. *Monthly Weather Review*, Vol. **118**, 1429-1443

Janjic, Z. I., 1994: The step-mountain eta coordinate model: further developments of the convection, viscous sublayer and turbulence closure schemes. *Monthly Weather Review*, Vol. **122**, 927-945.

Janjic, Z. I., 1997: Advection scheme for passive substances in the NCEP Eta model. *Research Activities in Atmospheric and Oceanic Modelling*, WMO, Geneva, CAS/JSC WGNE, 3.14.

Janjic, Z. I., 2002: A Nonhydrostatic Model Based on a New Approach. *Meteorology and Atmospheric Physics,* DOI 10.1007/s00703-001-0587-6.

Janjic Z. I., J. P. Gerrity, Jr. and S. Nickovic, 2001: An Alternative Approach to Nonhydrostatic Modeling. *Monthly Weather Review,* Vol. **129**, 1164-1178.

Koren V., J. Schaake, K. Mitchell, Q.-Y. Duan, F. Chen and J. Baker, 1999. A parameterization of snowpack and frozen ground intended for NCEP weather and climate models, J. Geophys. Res., 104, No. D16, 19569-19585.

Model for simulation of the sea salt aerosol atmospheric cycle

S. Nickovic, ICoD, University of Malta; now at: World Meteorological Organization, Geneva, Switzerland; Z.I. Janjic, NCEP, Washington DC, USA; P. Kishsha and P. Alpert, Tel-Aviv University, Israel; email: snickovic@wmo.org

There is an increasing interest in simulating various impacts of sea salt on the atmosphere, such as direct radiation effects and indirect effects on cloud formation. Sea salt aerosol is produced over the air-sea interface as a result of the air momentum transfer to the sea surface. The sea salt atmospheric process starts when strong winds generate whitecaps of the breaking waves with a high concentration of bubbles. Their bursting releases salt aerosol into the marine boundary layer. Once injected into the atmosphere, the sea salt is transported vertically and horizontally and it is deposited on the ground by wet and dry deposition.

In this article we describe a model for simulating the sea salt aerosol atmospheric cycle. This model (DREAM-SALT) is based on the DREAM dust aerosol model (Nickovic et al., 2001), which was adapted to function for sea salt aerosol. The NCEP/Eta regional atmospheric model (Janjic, 1994; Janjic, 2001; and references therein) drives the aerosol. The aerosol emission scheme is based on the viscous sublayer model (Janjic, 1994) in which energy and mass transfers above the air-sea interface critically depend on turbulent conditions. The Janjic viscous sublayer scheme is based on the following assumptions: (a) there are two distinct layers: a thin viscous sublayer immediately above the surface, and a turbulent layer above the viscous sublayer; (b) at the top of the viscous sublayer all fluxes are continuous. In the viscous sublayer, it is assumed that (1) the vertical transport is determined entirely by the molecular diffusion; and (2) vertical profiles of variables are linear since the viscous diffusivity is assumed to be constant. In the turbulent layer, the vertical transport is entirely defined by turbulent fluxes.

Depending on the Reynolds roughness number $\mathrm{Re} = z_0 u_* / \nu$, the viscous sublayer scheme is assumed to operate in three different regimes: smooth and transitional; rough; and rough with spray. Here, z_0, u_* and ν are the roughness height, friction velocity and the air viscosity, respectively. When Re exceeds a prescribed critical value Re_r, the flow ceases to be smooth and enters the rough regime. The rough regime is characterized by combined viscous and turbulent mixing. In the rough regime with spray, the mixing becomes fully turbulent. Here, the breaking waves provide a mass exchange, which is more effective than that of the two previous regimes. The values of u_* at which the transitions between the different regimes occur are $u_{*r} = 0.225\ ms^{-1}$ and $u_{*s} = 0.7\ ms^{-1}$.

Following Janjic (1994), the sea salt fluxes are defined by

$$F_{C(VSC)} = \nu \frac{C_{INT} - C_S}{z_{INT}}\ ; \ , \quad F_{C(TRB)} = K_C \frac{C_{LM} - C_{INT}}{z_{LM} - z_{INT}}$$

in the viscous and turbulent sublayers, respectively. Here, K_C is the Monin-Obukhov bulk turbulent mixing coefficient; C_S, C_{INT} and C_{LM} are sea salt concentrations at the sea surface, at the top of the viscous sublayer and at the first computational model layer, respectively; z_{INT} and z_{LM} are the heights of the top of the viscous sublayer and the first computational model layer, respectively. The depth of the viscous sublayer is calculated as

$$z_{INT} = \frac{0.35 M \sqrt[4]{R_r} \sqrt[2]{S_c}\, \nu}{u_*}$$

(Janjic, 1994). Here, S_c is the Schmidt number; the constant M has the value of 30 in the first regime and 10 in the second regime. The viscous sublayer depth z_{INT} decreases as the turbulence increases. The viscous sublayer vanishes in the last, rough regime with spray. From the requirement for continuity of the viscous and turbulent fluxes at the viscous/turbulent interface, it follows that $C_{INT} = \frac{C_S + \omega C_{LM}}{1+\omega}$, where $\omega = \frac{K_C z_{INT}}{\nu (z_{LM} - z_{INT})}$. Here ω plays the role of a weighting factor. Note that ω vanishes with the disappearance of the viscous sublayer in the rough regime with spray. As a consequence, it follows that $C_{INT} = C_S$ at $z = z_0$. In the Janjic scheme, the interface value C_{INT} is considered as the lower boundary condition for the surface turbulent scheme in the NCEP/Eta model.

In our approach, the aerosol concentration at the top of the viscous sublayer is used as the lower boundary condition, in contrast to most other sea salt models that use a flux form for the emission function (e.g. Monahan, 1986; Gong et al., 2003). In our 'concentration' boundary condition approach, effects of the viscous sublayer model are fully taken into account. Based on such concept, we have developed two alternate emission schemes.

The f*irst emission scheme* defines the lower boundary condition using the source function of Erickson et al. (1986):

$$C_S^j = 10^{-9}\alpha^j \exp(0.16U_{10} + 1.45) \qquad for \quad U_{10} \le 15\,ms^{-1}; \quad j = 1, N$$
$$C_S^j = 10^{-9}\alpha^j \exp(0.13U_{10} + 1.89) \qquad for \quad U_{10} > 15\,ms^{-1}; \quad j = 1, N$$

Here, U_{10} is the 10m wind intensity; $\alpha_j \in (0,1)$ is an array describing the source particle size distribution. In our model setup, we use $N = 8$ particle categories with sizes ranging from 1-8 μm. All variable units are given in the MKS system.

In the *second emission scheme*, the sea salt concentration on the top of the viscous sublayer is used as the lower boundary condition. It is assumed here that C_{INT} is proportional to the salinity of the predicted specific humidity q_{INT} at the same height:

$$C_{INT}^j = 10^{-3}\alpha^j S q_{INT} \rho_{air}$$

where, S is the sea water salinity; ρ_{air} is the air density. Again, variable units are in the MKS system.

Preliminary experiments with the sea salt model based on real-time atmospheric forecasts indicate that both emission schemes proposed in this study reproduce major observed features of sea salt aerosol, such as horizontal and vertical concentration distribution. Figure 1 shows 24-hour predicted horizontal distributions of surface sea-salt concentration and wind at 3000 m over the Mediterranean region on August 2, 2006. In Figure 2, time evolution of the sea salt concentration over the sea near the west coast of Africa is displayed. More extensive tests in the future will demonstrate which of the two proposed schemes more accurately simulate the sea salt process.

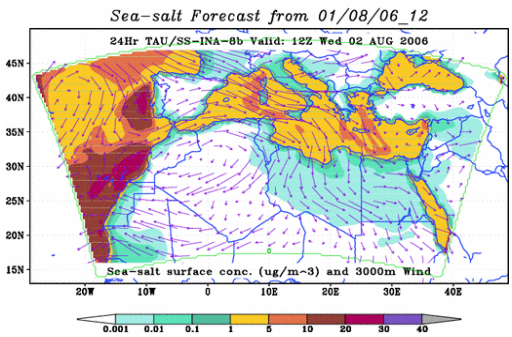

Fig. 1.

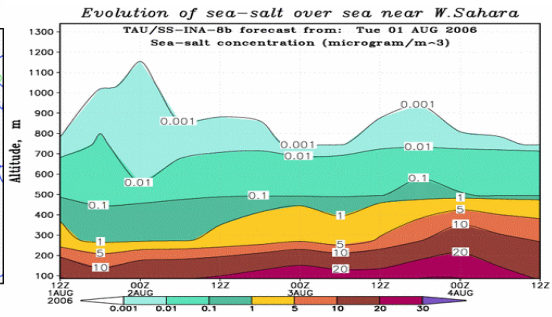

Fig. 2.

ACKNOWLEDGEMET

Major developments of the aerosol transport component were performed within the 4th Italo-Maltese Protocol (1995-2000).

REFERENCES

Gong, S.L., A parameterization of sea-salt aerosol source function for sub- and super- micron particles, Global Biogeochemical Cycles, 17 (4), 1097, doi:1029/2003GB002079, 2003.

Janjic, Z. I., 1994: The step-mountain eta coordinate model: further developments of the convection, viscous sublayer and turbulence closure schemes. *Monthly Weather Review*, Vol. **122**, 927-945.

Janjic, Z. I., 2001a: Nonsingular Implementation of the Mellor-Yamada Level 2.5 Scheme in the NCEP Meso model. NOAA/NWS/NCEP Office Note #437, December 2001, 61 pp.

Nickovic, S., G. Kallos, A. Papadopoulos and O. Kakaliagou, 2001, A model for prediction of desert dust cycle in the atmosphere, J. Geophys. Res., 106, 18113-18129.

Monahan, E. C., D. E. Spiel, and K. L. Davidson, A model of marine aerosol generation via whitecaps and wave disruption, in *Oceanic Whitecaps and Their Role in Air-Sea Exchange*, edited by E. C. Monahan and G. Mac Niocaill, pp. 167–174, D. Reidel, Norwell, Mass., 1986.

Assessing global model hydrology with simulations from the Stable Water-isotope Intercomparison Group

David Noone (dcn@colorado.edu)
Department of Atmospheric and Oceanic Sciences, and
Cooperative Institute for Research in Environmental Sciences
University of Colorado, Boulder, CO, USA

The atmospheric water cycle in climate models has developed far beyond the pioneering scheme by Manabe *et al.* (1965) to now include elaborate land surface exchange, sophisticated cloud physics and convection. While present generation climate models credibly reproduce the observed distribution of water vapour, there remains a question as to whether this results from the correct balance of contributing processes. Indeed the different ways various models reach hydrologic balance is likely key to understanding the range of climate sensitivities found in model intercomparisons. The Stable Water-isotope Intercomparison Group (SWING) brings together modeling groups with GCMs capable of simulation the isotopic composition of water to deduce differences in the atmospheric hydrology and exchange processes in climate models though isotope simulations.

Figure 1 shows the June-July-August mean isotopic composition of water vapour at 700 hPa from the three models participating in the SWING Phase 1 experiment (Hoffmann *et al.* 1998, Noone and Simmonds 2002, Schmidt *et al.*, 2005). The experiment protocol includes prescribed climatological sea surface temperatures and greenhouse gas concentrations set to 1990s levels. Each of the models simulates the isotopic composition of precipitation very well, yet there are substantial biases in the simulation of tropospheric vapour. The models agree that vapour is more depleted at higher latitudes where condensation has preferentially removed heavy nuclides. The model simulations are less similar in locations where convection is common. The models show more depletion in regions of intense convection where condensation processes dominate, but show local enrichment where convection acts to loft non-depleted vapour from the boundary layer. The degree to which these affect the simulated hydrology is seen in the isotopes. One model has less depleted water in the tropics which is linked to excessive convective transport, while another model has more localized features where convection is more closely tied to the geography. These model results can be compared to measurements derived from the Tropospheric Emission Spectometer (Worden *et al.*, 2007). This is the first global tropospheric survey of isotopic composition and provides an unprecedented and important ground truth for isotope models. The difference between the all models and the observations is larger than the difference between any two models. Some of this discrepancy is associated with sampling biases and resolution differences between the models and the observations; however, the mismatch also indicates that the way in which each of the models achieves hydrologic balance is through a different combination of contributing processes (evaporation, transpiration, boundary layer mixing, large-scale advection and condensation). As such, we have demonstrated the independent information provided by isotopes has great utility in ensuring the atmospheric water balance in models is obtained for the right reasons.

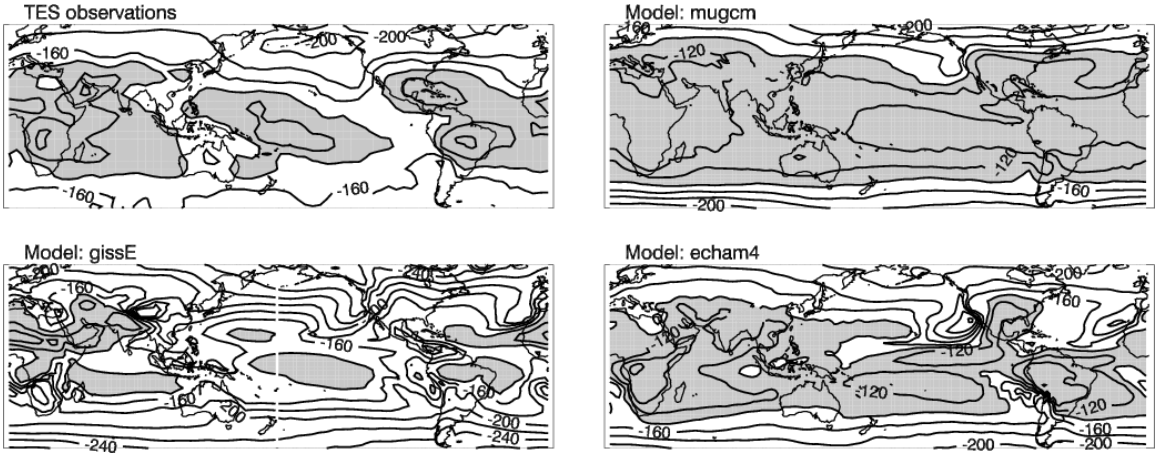

Figure 1: June-July-August mean isotopic composition of water vapour (δHDO) at 700 hPa from the Tropospheric Emission Spectrometer, and simulated by three general circulation models. Values are shown as a normalized difference from the isotopic composition of ocean water. Contour interval is 20 permil, and values larger than -140 permil are shaded.

References

Hoffmann, G., M. Werner, and M. Heimann, The water isotope module of the ECHAM atmospheric general circulation model - a study on time scales from days to several years, *Journal of Geophysical Research*, 103 (D14), 16871-16896, 1998.

Manabe, S., J. Smagorinsky and R. F. Strickler. Simulated climatology of a general circulation model with a hydrologic cycle, Mon. Wea. Rev. 93, 769-798, 1965.

Noone, D., and I. Simmonds, Associations between delta O-18 of water and climate parameters in a simulation of atmospheric circulation for 1979-95, *Journal of Climate*, 15 (22), 3150-3169, 2002.

Schmidt, G.A., G. Hoffmann, D.T. Shindell, and Y. Hu: Modelling atmospheric stable water isotopes and the potential for constraining cloud processes and stratosphere-troposphere water exchange, *J. Geophys. Res.*, 110, D21314, doi:10.1029/2005JD005790, 2005.

Worden, J. R., D. Noone, K. Bowman and TES Team Members, Importance of rain evaporation and continental convection in the tropical water cycle, *Nature*, 445, 528-532, doi:10.1038/nature05508, 2007.

SWING data archived and available at http://atoc.colorado.edu/~dcn/SWING

Shallow cumulus parameterisation in the CRCM

Cynthia Papon⋆ papon@sca.uqam.ca
Colin Jones⋆ jones.colin@uqam.ca
Dominique Paquin† paquin.dominique@ouranos.ca
Yanjun Jiao⋆ jiao.yanjun@uqam.ca

⋆CRCMD-UQAM
†OURANOS
550, Sherbrooke E., Montréal

ABSTRACT

Shallow cumulus are ubiquitous over the tropical ocean and mid-latitude summer time boundary layer. They impact the thermodynamic structure of the lower atmosphere and, through interaction with solar radiation, influence the surface energy budget. In this work, we implement a physically based parameterisation of shallow cumulus cloud fraction and couple this with the Bechtold-Kain-Fritsch convection scheme. The scheme is incorporated into the 3D Canadian Regional Climate Model (CRCM) and the representation of shallow cumulus convection and associated cloud fields evaluated over the tropical Pacific following the Pacific Cross-Section Intercomparison (GPCI) experiment protocol.

1 SHALLOW CLOUD COVER PARAMETERISATION

Albrecht's parameterisation assumes that the decay time of shallow cumulus controls their fractional cloud cover. This decay time depends on the difference of humidity between the cloud and its environment. The total specific humidity of the shallow convective cloud is the sum of q_0, the vapor in the convection plume, and l_0, the liquid water in the plume. The mean specific humidity in the parcel $\bar{q}$ is used to represent the environment, and $\bar{q_s}$ denotes the mean saturation specific humidity. Two variables are then defined:

- the mean relative humidity in the parcel $RH = \frac{\bar{q}}{\bar{q_s}}$
- the virtual relative humidity of the cloud if all water is evaporated at constant temperature $SR = \frac{q_0 + l_0}{\bar{q_s}}$

The cloud cover (σ) is computed as the ratio between the virtual sursaturation of the cloud and the difference of relative humidity between the convection cloud and its environment:

$$0 \leq \sigma = \frac{SR - 1}{SR - RH} \leq 1 \qquad (1)$$

2 GPCI EXPERIMENT IN THE CRCM

We implement this parameterisation in the CRCM, following the GPCI experimentation. We see the region of study in figure 1: the simulation grid is in navy blue and , in clear blue, is the results region: the rectangle for the 2 dimensions variables and the dotted line for cross-sections.

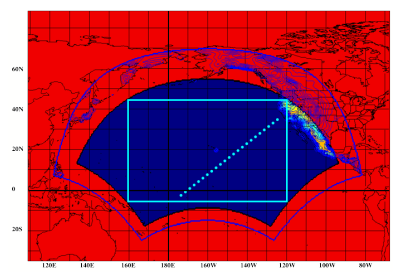

Figure 1: Region of study for the GPCI experiement.

Only cross-sections will be presented and compared to the ECMWF reanalysis (graphics taken from the paper of Siebesma and al. [1]). The period of interest is June, July and August 1998 (JJA98). CRCM uses a 180km resolution grid at 60^oN, with 29 vertical levels and 15mn timestep.

Looking at figure 2, which represents the subsidence ω, 3 regions are distinguishable: from mid-latitudes to 29° is a region of strong subsidence (R1), after which we have light subsidence, corresponding to the shallow convection region (R2), up to the region of deep convection (R3). The latitudes at which these regimes happen are in accordance with the ECMWF reanalysis, so we know we have shallow convection happening in the good regions.

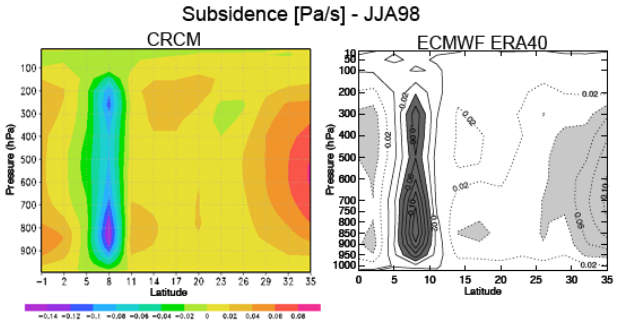

Figure 2: Subsidence for the CRCM and ECMWF reanalysis.

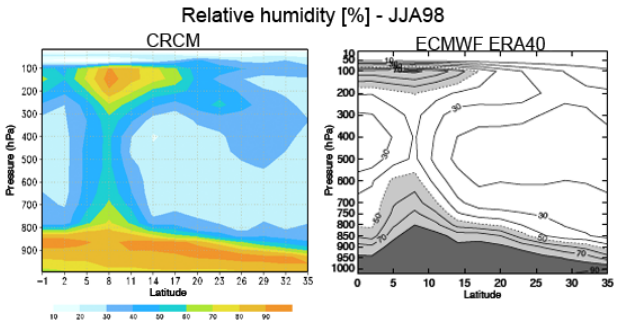

Figure 3: Vertical profile of the relative humidity for the CRCM and the ECMWF reanalysis.

Figure 3 shows that, for the R2 regions, the relative humidity is overestimated by 10% at the top of the boundary layer, and underestimated by 10% at the surface. Similarly, the liquid cloud water is overestimated in the same regions (not shown), and impacts directly the cloud cover (figure 4) which is overestimated by 15 to 20% in these regions. According to the results in the paper of Bony and Dufresne [5], the shallow clouds cover (figure 5) is overestimated by 15%, and is probably the main contribution to the overall cloud cover overestimation.

3 Discussion

In this work, we tested a diagnostic parameterisation of the cumulus cloud cover. This parameterisation is physically related to the shallow convection, and therefore influenced by its parameters, mainly the humidity. It appears that Albrecht's parameterisation gives a reasonnably accurate representation of the cloud cover in a parcel. The cloud cover is overestimated by approximately 15%, which seems to be directly related to the vertical distribution of the humidity of the shallow convection. The integration of such a parameterisation in a Regional Model is important for the transferability, particularly in the Trades where the shallow convection is the dominant regime.

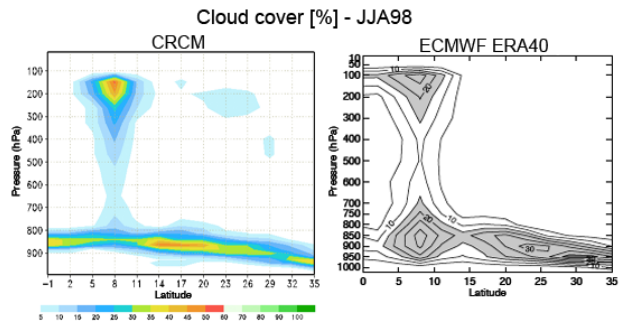

Figure 4: Vertical profile of the cloud cover for the CRCM and the ECMWF reanalysis.

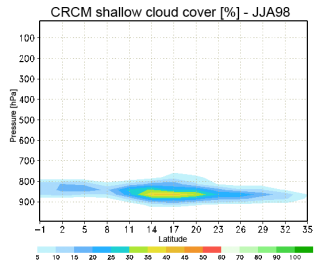

Figure 5: Vertical profile of the shallow cumulus cloud cover for the CRCM

References

[1] Siebesma A. Pier and al. Cloud representation in general circulation models over northern pacific ocean: a eurocs intercomparison study. *Monthly Weather Review*, 127:341–362, 1999.

[2] Caya D. and R. Laprise. A semi-implicit semi-Lagrangian regional model: the Canadian RCM. *Monthly Weather Review*, 127:341–362, 1999.

[3] Kain J.S. The Kain-Fritsch convective parameterization: an update. *Journal of Applied Meteorology*, 43:170–181, 2004.

[4] Bechtold P., Bazile E., F. Guichard, P. Mascart, and E. Richard. A mass-flux convection scheme for regional and global models. *Quarterly Journal of the Royal Meteorological Society*, 127:869–886, 2001.

[5] Bony S. and Dufresne J.L. Marine boundary layer clouds at the heart of tropical cloud feedback uncertainties in climate model. *Geophysical Research Letters*, 32, 2005.

Climate Model Capability in Resolving Diurnal Cycle of Rainfall

D. W. Shin, S. Cocke, T. E. LaRow, and Y.-K. Lim
Center for Ocean-Atmospheric Prediction Studies, Florida State University, Tallahassee, FL, USA
(shin@coaps.fsu.edu)

An investigation is carried out to study the model capability in resolving the diurnal cycle of June-August rainfall using the Florida State University/Center for Ocean-Atmospheric Prediction Studies (FSU/COAPS) climate model (Cocke and LaRow, 2000) and to examine the role of the diurnal cycle in seasonal precipitation simulations. The Tropical Rainfall Measuring Mission multi-satellite precipitation analysis products (TMPA, Huffman et al., 2006) are used as the verification data. In order to uncover which model components are more responsible for the diurnal cycle, a number of seasonal (3-month long) integrations are performed by modifying the climate model configurations.

The observational intensity, in terms of standard deviation, of the diurnal cycle is shown in Fig. 1a. Well-known intense diurnal cycle regions over land can be easily detected. Moderate, but not negligible, diurnal variability is clearly apparent over the ocean, especially along the ITCZ. The corresponding intensities from the five model configurations are illustrated in Fig. 1 as well. While the default FSU/COAPS model with the MIT (Fig. 1f) produces an extremely strong diurnal variability over land, other model configurations generate somewhat weaker diurnal variability compared to the TMPA observation. The diurnal cycle over the oceanic ITCZ is, to some extent, captured only by the NRL at this resolution (T63). Similar intensity maps but for the T255 horizontal resolution are shown in Fig. 2. Although overall results are analogous to the T63 runs, the high resolution runs provide much more detailed diurnal variability and improve the diurnal cycle signal over several regions. In particular, the missed diurnal cycle over the oceanic ITCZ is now somewhat captured even in the CCM3, the NCEP, and the NCAR. Seasonally averaged 3-hourly precipitation evolutions are shown in Fig. 3 in order to assess the phase of precipitation amount from the observation and the models at six selected regions (see Fig. 1a). The five model configurations are the same as those used in Fig. 1. While the late afternoon maxima are clearly shown from the TMPA data over the southeast USA, Indochina Peninsula, and the NAME region, the well-known late night maximum is apparent over the central United States. The diurnal cycle over the ocean exhibits two maxima (the early morning and afternoon) with relatively small magnitude. All of the models produce different phases of diurnal cycle depending on the location. However, the MIT scheme always produces a strong diurnal cycle with the maximum rainfall around the local noon time, regardless of land locations. This implies that the MIT scheme intrigues the most intensive convective activities whenever there is strong incoming solar radiation.

It is found that the convective scheme employed is the most crucial component in properly capturing the diurnal cycle of rainfall. A detailed and improved signal of diurnal cycle is obtained in the experiments with a higher horizontal resolution. A negative influence is found when the Community Land Model version 2 as a land surface scheme is used. No improvement in the oceanic diurnal cycle is discovered even if a frequently coupling ocean model is used rather than prescribed sea surface temperatures. It is also shown that the model configuration which resolves the diurnal cycle better provides an improved seasonal precipitation forecast.

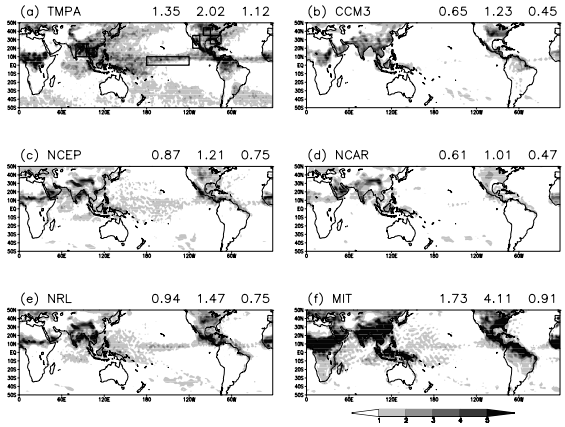

Fig. 1: An observed standard deviation (i.e., intensity, mm d^{-1}) of rainfall diurnal cycle from the TMPA (a) is compared with those of seasonal precipitation forecasts from (b) CCM3, (c) NCEP, (d) NCAR, (e) NRL, and (f) MIT. The horizontal resolution is T63 (~1.875°). Area averaged (50 °S-50 °N) values (first: land and ocean, second: land only, third: ocean only) are shown in the upper right corner.

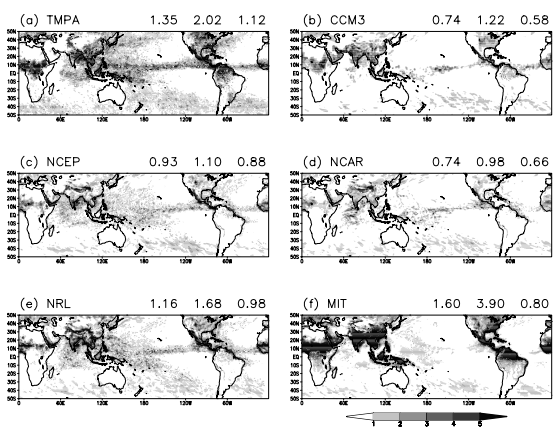

Fig. 2: As in Fig. 1, but for the T255 (~0.469°) horizontal resolution. The resolution of CCM3 is T126 (~0.938°).

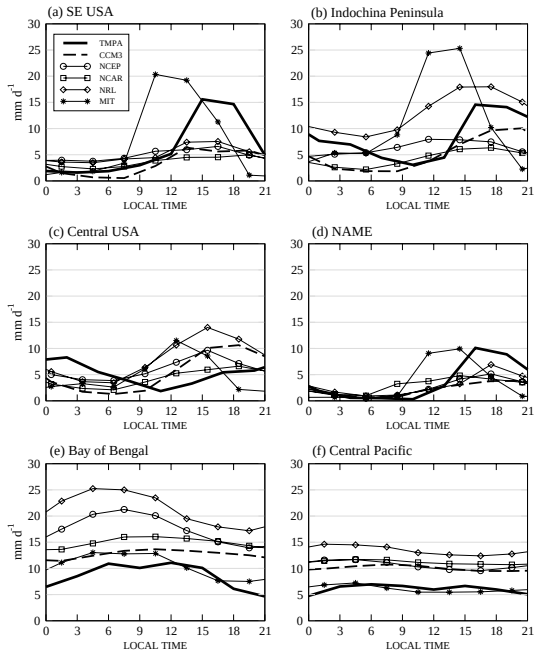

Fig. 3: Diurnal cycles of area-averaged precipitation amount (mm d^{-1}) at six different regions. The abscissa is LST. The regions examined are (a) the southeast United States (25°N-35°N, 90°W-75°W), (b) Indochina Peninsula (10°N-20°N, 95°-110°E), (c) the central United States (35°N-44°N, 100°W-90°W), (d) the North American Monsoon Experiment area (20°N-35°N, 115°W-105°W), (e) Bay of Bengal (10°N-25°N,80°-95°E), and (f) the central Tropical Pacific (0°-10°N, 180°-120°W).

Acknowledgements

Computations were performed on the IBM SP4 at the FSU. COAPS receives its base support from the Applied Research Center, funded by NOAA Office of Global Programs awarded to Dr. James J. O'Brien.

References

Cocke, S., and T. E. LaRow, 2000: Seasonal predictions using a regional spectral model embedded within a coupled ocean-atmosphere model. *Mon. Weather Rev.*, **128**, 689-708.

Huffman, G. J., R. F. Adler, D. T. Bolvin, G. Gu, E. J. Nelkin, K. P. Bowman, Y. Hong, E. F. Stocker, and D. B. Wolff, 2007: The TRMM Multisatellite Precipitation Analysis (TMPA): Quasi-global, multiyear, combined-sensor precipitation estimates at fine scales. *J. Hydrometeor.*, in press.